ROYAL SOCIETY OF CHEMISTRY

Journal of Materials Chemistry A

ARTICLE

Journal of Materials Chemistry A Accepted Manuscript

Synthesis of Sn/MoS₂/C composite as high-performance anode for Lithium-ion batteries

Qing-Yu Li[a], Qi-Chang Pan[a], Guan-Hua Yang[a], Xi-Le Lin[a], Zhi-Xiong Yan[a], Hong-Qiang Wang*,[a,b], and You-Guo Huang*,[a]

Tin (Sn) has been considered as one of the most promising anode materials for high-performance lithium ion batteries (LIBs) due to its high theoretical capacity, abundance and low toxicity. However, fast capacity fading and poor rate capability hinder its application in LIBs. Herein, we reported a novel composite consisting of few-layer MoS₂ and Sn nanoparticles is synthesized as an anode for LIBs. In such composite anode, MoS₂ nanosheets provide flexible substrates for the nanoparticles decoration, accommodating the volume changes of Sn during the cycling process. While Sn nanoparticles also can act as spacers to stabilize the composite structure and make the active surfaces of MoS₂ nanosheets accessible for electrolyte penetration during the charge/discharge process. Electrochemical measurements demonstrated that the Sn/MoS₂/C composite exhibits extremely long cycling stability even at high rate (a reversible capacity of 624.5 mAh g⁻¹ at a current density of 1 A g⁻¹ after 500 cycles) and superior rate capability (1050 mAh g⁻¹ at 100 mA g⁻¹, 895 mAh g⁻¹ at 200 mA g⁻¹, 800 mAh g⁻¹ at 500 mA g⁻¹, 732 mAh g⁻¹ at 1 A g⁻¹ and 630 mAh g⁻¹ at 2 A g⁻¹).

Introduction

High-performance lithium-ion batteries (LIBs) have attract attention as a power supply for hybrid electric vehicles, electric vehicles and portable electronic devices due to their high voltage, long cycle life, environmental friendliness and high energy-density.[1,2] Although currently commercial graphite anode has been considered as one of the excellent anode materials for LIBs, however, graphite, is far from meeting the requirements for high energy/power density because of its low theoretical specific capacity (372 mA h g⁻¹) and poor rate capability.[3] Therefore, to satisfy the ever-growing power requirements of the markets, much efforts has been devoted to developing anode materials with high capacity, long cycle life, and high rate capability.[4,5] Among all the candidates anode materials, such as Si-based anode materials,[6,7] Sn-based anode materials[8,9] and transition metal oxides,[10,11] et al. Sn-based materials have been considered as most promising substitute for graphite owing to their high theoretical capacity, high operating potential and low toxicity.[12] However, the practical application of Sn-based materials suffers from its pulverization problem caused by the huge volume change during lithiation/delithiation process, which results in fast capacity

[a] *Guangxi Key Laboratory of Low Carbon Energy Materials, School of Chemical and pharmaceutical Sciences, Guangxi Normal University, Guilin, 541004, China*

[b] *Hubei Key Laboratory for Processing and Application of Catalytic Materials, Huanggang Normal University, Huanggang 438000, China*

Corresponding authors
E-mail addresses:
* *Hong-Qiang Wang, whq74@126.com, Fax: +86-0773-5858562*
* *You-Guo Huang, huangyg72@163.com*

fade.[13]

Metallic tin (Sn), one of the most promising anode materials for high-performance LIBs due to its high theoretical capacity (991 mA h g⁻¹ or 7313 mA h cm⁻³).[14] But the huge volume change resulting in fast capacity fade imposes restrictions on application in LIBs. To circumvent this problem, much efforts have been made to improve the structural stability, previous reports have shown that decreasing the dimension of Sn into nanometer range could reduce the mechanical stress during the charge and discharge process.[15,16] In addition, the nanostructured materials could provide high rate capability owing to they could shorten the path lengths for Li-ion transport at the expense of the aggregation of Sn nanoparticles resulting in poor cyclability. In order to solve these problems, various Sn/C hybrids such as Sn nanoparticles encapsulated with carbon nanotubes,[17] Sn nanoparticles embedded in carbon[18,19] and Sn@C nanocomposite[20,21] have been designed. These carbons not only can provide spaces to buffer the mechanical stress induced by the volume change but also can enhance the electrical conductivity of the composite, contributing to significantly improved cycling performance and rate capability.

Recently, molybdenum disulfide (MoS₂), a transition metal sulfide, which consists of a graphene-like layered structure with S-Mo-S forming covalent bond within each plane and connected through van der Waal,s interactions among adjacent planes.[25] This structure allows lithium ion to freely move within the space and with low volume expansion and contraction, additionally, monolayer MoS₂ have a high mechanical strength, which is comparable to steel.[26] So such strong mechanical behavior helps MoS₂ nanosheets to accommodate the severe structural deformation of the metal oxide

incorporated during the lithiation/delithiation process. Hence, many MoS_2 directly decorated metal oxide composite have been developed as the anode materials for LIBs, such as SnO_2/MoS_2 composites,[27] Fe_3O_4/MoS_2 composites,[28] MoS_2/SiO_2/graphene hybrids,[29] and so on.

In this paper, we report a very facile and easy method to fabricate Sn nanoparticles embedded with few-layer MoS_2 under mild conditions and use them as electrode materials for LIBs. By introduced the Sn nanoparticles into MoS_2 nanosheets, trying to combine their merits, the Sn nanoparticles serve as spacers to prevent the restacking of adjacent MoS_2 nanosheets. Moreover, the MoS_2 nanosheets not only can sever as a substrate and prevent the agglomeration of Sn nanoparticles but also can buffer the volume change of the Sn. When the composite is evaluated as an anode material for LIBs, which exhibits a reversible capacity of 624.5 mAh g^{-1} at a current density of 1 A g^{-1} after 500 cycles. On the other hand, this composite also gives a superior rate performance of 630 mAh g^{-1} at 2 A g^{-1}.

Experimental

Synthesis of MoS_2/C composite

The MoS_2/C composite was synthesis according to the literature,[30] in a typical synthesis, 3 g of $Na_2MoO_4 \cdot 2H_2O$ and 4 g NH_2CSNH_2 were dissolved in 400 ml deionized water, and then 10 g of glucose was added into the solution. After stirring for a few minutes, the obtained clear solution was transferred into a 500 ml Teflon-lined stainless steel autoclave and sealed tightly, heated at 240 °C for 24 h. After cooling naturally, the black precipitates were collected by filter, washed with deionized water, and dried oven at 80 °C for 12 h. The MoS_2/C composite were annealed in a conventional tube furnace at 800 °C for 2 h under Ar atmosphere.

Preparation of Sn/MoS_2/C composite

0.6 g MoS_2/C composite was added to 60 ml ethanol-water (1:1, v) mixed solution, followed by the addition of 1.5 g $Na_2SnO_3 \cdot 3H_2O$ and 4 g urea. After stirred for 1h, this suspension was transferred into a 100 ml Teflon-lined stainless steel autoclave, and then placed in an oven at 200 °C for 18h. After that, SnO_2/MoS_2/C composite was obtained by filter, washed with deionized water three times and then dried in an oven at 80 °C overnight. This composite was then dispersed in 60 ml ethanol-water (1:1, v) mixed solution containing 3 g glucose, transformed into 100 ml autoclave, and kept at 180 °C for 18 h. The precipitate was collected by filter and washed with water three times. After dried at 80 °C, the powder was finally calcined at 700 °C under Ar atmosphere for 4 h, then the Sn/MoS_2/C composite was obtained. For comparison, Sn/C composite were also synthesized by hydrothermal method and without add MoS_2 at the same conditions.

Characterization of materials

The microstructure of the Sn/MoS_2/C composite was characterized by a filed emission scanning electron microscope (SEM, Philips, FEI Quanta 200 FEG) and transmission electron microscope (TEM, JEOL 2011). The phase identification of the composites was conducted by an X-ray diffractometer (XRD, Rigaku D/max 2500) with Cu Kα radiation at 40 kV and 40 mA

from 10°-90° with a step size of 0.02° and step time of 5 seconds. The crystal and composition were characterized by laser Raman spectroscopy (Jobin Ybon, T6400). X-ray photoelectron spectroscopy (XPS) experiments were carried out using an AXIS ULTRA DLD instrument, using aluminum Kα X-ray radiation during the XPS analysis. The carbon content was determined from thermogravimetric analysis (TGA) (Nitzsch STA 449 C) at a heating rate of 5 °C min^{-1}. The exact Mo:Sn molar ratio in the composite was also measured by inductively coupled plasma optical emission spect-roscopy (ICP-OES, Agilent 730). The result measured for the presence of Mo and Sn element (molar ratio: Mo : Sn = 0.52: 1.2) by TCP-OES.

Electrode preparation and electrochemical measurements

The electrode was made from a mixture of the active materials, super P (SP) and polyvinylidene fluoride (PVDF) in a weight ratio of 80 : 10 : 10. The mixture was dispersed in N-methyl-2-pyrrolidone (NMP) to form homogeneous slurry, and then the slurry was pasted on to a copper foil and completely before use, and the working electrode with active material loading of 0.8 mg cm^{-2}. For electrochemical testing, CR2025-type coin cell were assembled in an argon-filled glove box. Li metal foil was used as a counter electrode, 1 mol L^{-1} $LiPF_6$ in mixed solution of ethylene carbonate (EC) and dimethyl carbonate (DMC) (1:1, v/v) was used as the electrolyte, and Celgard 2200 as the separator. Galvanostatic charge-discharge test was conducted within cut-off voltages from 0.01 to 3.0 V at 25 °C using Land battery measurement system (LAND BT2013A, Wuhan, China). Cyclic voltammetry (CV) was carried out on an electrochemical workstation (IM6, Germany) in a voltage range of 0.01-3.0 V at a scan rate of 0.1 mV s^{-1}.

Results and discussion

Fig. 1 shows a schematic of the synthesis route of Sn/MoS_2/C composite. Firstly, the MoS_2/C composite was produced by the hydrothermal reaction between $Na_2MoO_4 \cdot 2H_2O$, NH_2CSNH_2 and glucose, and then annealing at 800 °C in Ar. Secondly, the obatined MoS_2/C composite was highly dispersed in the ethanol-water (1:1, v) solution, and then addition of $K_2SnO_3 \cdot 3H_2O$ and urea, after hydrothermal at 200 °C for 18 h the SnO_2/MoS_2/C composite was obtained, SnO_2 was generated during the Kirkendall process of MoS_2/C, inserted into and encapsulated by few-layer MoS_2 which can prevent the SnO_2 nanoparticles (NPs) aggregation. Finally, introduced glucose into the SnO_2/MoS_2 composite and then glucose was carbonized at 700 °C under Ar atmosphere for 4h, the glucose is transformed into thin carbon layer coating the surface of the SnO_2 and at the same time the carbon reduced the SnO_2 to Sn, therefore, the Sn/MoS_2/C composite were obtained.

Fig. 2 A shows the X-ray diffraction (XRD) patterns of MoS_2/C composite and Sn/MoS_2/C composite. Two diffraction peaks at 2θ= 33.5° and 59.1°, corresponding to the (100) and (110) planes of MoS_2. The absence of MoS_2 (002) reflection in MoS_2/C composite, which are the dominant peaks for a layered MoS_2 crystal, suggesting that there is hardly any stacking of MoS_2 in the c direction even after annealing. So the annealing is effective for improving the in-layer crystallinity of MoS_2 in the composite.[31.32] And also can see that the X-ray diffraction patterns of the Sn/MoS_2/C composite. In addition

to the (100) and (110) planes of MoS_2 in the Sn/MoS_2/C composite, all peaks of the diffraction patterns can be assigned to metallic tin, and no peaks of tin oxides can be found, it indicates that all of the tin oxides was reduction during the carbonization process. Which conform to the previous reports showing a temperature higher than 600 °C that can completely reduce tin oxides by carbon in an inert a-
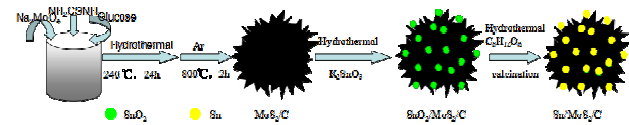
Fig. 1 Schematic illustration of the fabrication process.

tmosphere.[33] The Raman spectrum of the Sn/MoS_2/C composite located at 379 and 405 cm^{-1}. The difference (Δ) between these two Raman peaks can be used to identify the number of MoS_2 layers. The obtained Δ value is 26 cm^{-1}, indicating that MoS_2 has a few-layers structure.[34] In addition, two prominent peaks are also observed at 1345 cm^{-1} (D-band) and 1573 cm^{-1} (G-band), which are typical bands of carbonaceous. These above mentioned results further confirm that the obtained composite comprises few-layer MoS_2 and carbon.
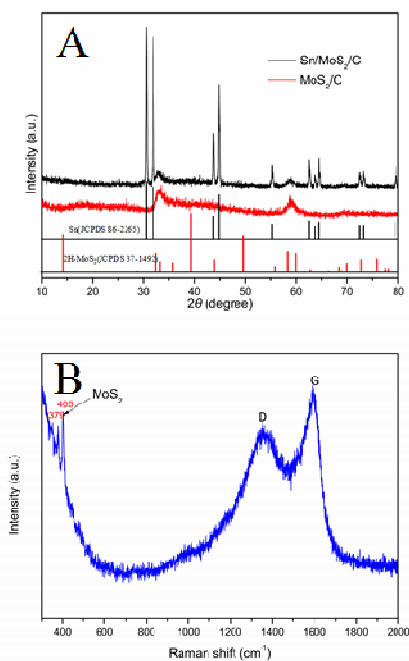
Fig. 2 (A) XRD patterns of Sn/MoS_2 /C composite and MoS_2/C composite and (b) Raman spectra of the Sn/MoS_2/C composite

The Sn/MoS_2/C composite is also confirmed by using X-ray photoelectron spectroscopy (XPS) analysis. Fig. 3A shows the survey XPS spectrum of Sn/MoS_2/C composite, which suggests the presence of Sn, Mo, S, C and O elements. The high-resolution spectrum of Sn 3d is shown in Fig. 3B. Two peaks located at 495.8 eV and 487.3 eV could be assigned to the binding energy of Sn $3d_{3/2}$ and Sn $3d_{5/2}$, respectively. The result indicates that the Sn element detected exists as Sn^{4+} state, which could be explained that Sn

particles on the surface of Sn/MoS_2/C composite have been oxidized in air during analysis.[2] Moreover, according to the above XRD analysize, most of Sn nanoparticles in composite have not been oxidized. Fig 2C, D shows the high-resolution spectrum of Mo 3d and S 2p, two peaks located at 232.5 eV and 229.3 eV could be assigned to the binding energy for Mo $3d_{3/2}$ and Mo $3d_{5/2}$, respectively. While S 2s with a broadened low intensity peak can be observed in the same spectrum. Such Mo peaks corresponded to +4 oxidation state, confirming presence of MoS_2 in the composite. The peaks for S 2p were resolved into two distinctive doublets, which were S $2p_{1/2}$ and S $2p_{3/2}$ peaks at 163.3 and 161.9 eV, respectively.[27] All these indicates that we successfully prepared Sn/MoS_2/C composite.
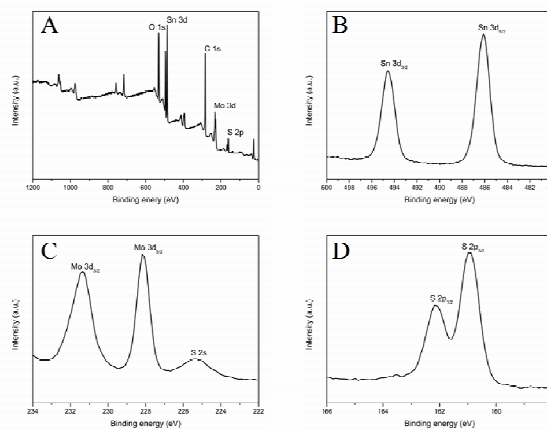
Fig. 3 (A) XPS survey spectrum, high resolution XPS spectra of (B) Sn, (C) Mo and (D) S of Sn/MoS_2/C composite.
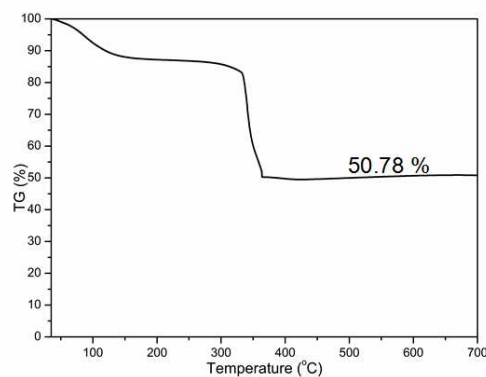
Fig. 4 TGA curves of Sn/MoS_2/C composite.

The content of Sn in the Sn/MoS_2/C composite was confirmed by the thermo-gravimetric analysis (TGA) in dry air. The TGA curves of Sn/MoS_2/C composite are shown in Fig. 4. The one continuous weight loss in the range of approximately 150-350 °C for the Sn/MoS_2/C composite is attributed to the oxidation of MoS_2 to MoO_3, the Sn to SnO_2 and the decomposition of amorphous.[35] Based on the TG result and the ICP-OES result of the Mo : Sn molar ratio of 1 : 2.31, the mass fraction of Sn, MoS_2 and C in Sn/MoS_2/C composite can be calculated around 29 %, 16 % and 55 %, respectively.

ARTICLE   Journal Name

The morphologies of the MoS_2/C composite by hydrothermal route and annealed are shown in (Fig. 5A, B). The SEM images give a general view of the morphology of the products over a large area. As is shown in (Fig. 5A, B) that the morphologies of the MoS_2/C composite prepared by hydrothermal and annealed which exhibit a sphere-like or three-dimensional architecture with a rough surface. It is reported that the carbonaceous materials produced by hydrothermal carbonization of glucose are sphere-like architectures.[36] Therefore, we acknowledge that glucose play a important role in the construction sphere-like or three-dimensional architecture of MoS_2/C composite in the hydrothermal process.
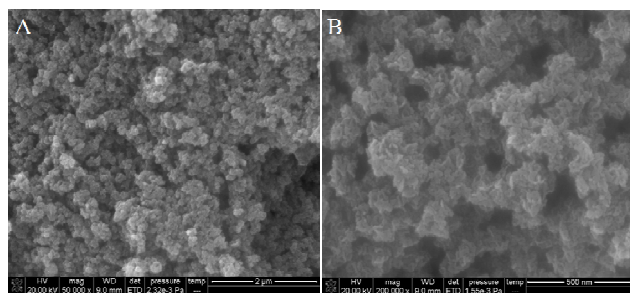
Fig. 5 SEM images of MoS_2/C composite.
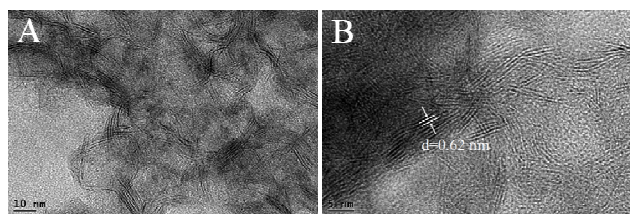
Fig. 6 TEM images of MoS_2/C composite

To further observe the microstructure, the MoS_2/C composites are characterized by TEM. Fig. 6 A, B shows the TEM images of the annealed the MoS_2/C composite. We can clearly seen that the MoS_2 nanoclusters comprised of few-layer-MoS_2 dispersed in amorphous carbon, Fig. 6 B exhibits clear lattice fringe for the composite, the spacing of the adjacent lattice planes is 0.62 nm, corresponding to planes of MoS_2 crystal, which is in agreement with the above XRD and Raman results.

Fig. 7 sho ws the Sn/MoS_2/C composite that after hydrothermal and carbonization under 700 °C in an Ar atmosphere, Fig. 7 A, B shows that the surface morphology of the Sn/MoS_2/C composite varies from the few-layer MoS_2/C composite, and it can clear see that (in Fig. 7A, B) some particles are distributed in the surface of the MoS_2/C composite in comparable to Fig 5 A, B. As can be seen in Fig. 6 C, D, we can see that some spherical nanoparticles with a diameter about 100 nm. The nanoparticles do not agglomerate in the MoS_2/C composite matrix even the nanoparticles size exceed 100 nm. According to the XRD, these nanoparticles may be Sn nanoparticles. In addition, it also can be seen clearly that the sphere-like or three-dimensional architecture of the MoS_2/C composite in the surrounding of the Sn nanoparticles, that indicating that the sphere-like or three-dimensional architecture of the MoS_2/C were not

changed after hydrothermal and calcination under Ar atmosphere at 700 °C.

The morphology of the as-prepared Sn/MoS_2/C composite is further characterized using transmission electron microscopy (TEM). As shown in Fig. 8 A, B, Sn NPs (black dots) were homogeneously embedded in the layer-structure MoS_2/C composite is observed, in good agreement with the SEM observations above. Fig. 8 C shows that it can see clearly that the Sn NPs were coated with thin carbon layer and then encapsulated by few-layer MoS_2 tightly. Fig. 8 D exhibit clear lattice fringe for the core, the spacing of the adjacent lattice planes is 0.29 nm, corresponding to (200) planes of Sn crystal, indicating that the inner core in pure metallic Sn.
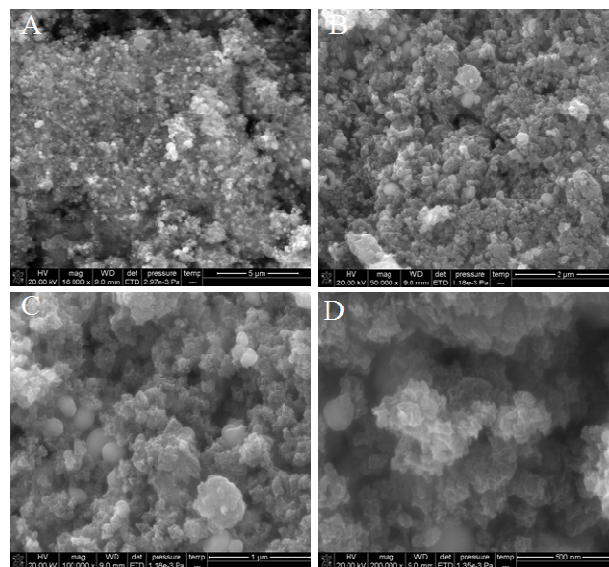
Fig. 7 SEM images of the Sn/MoS_2/C composite
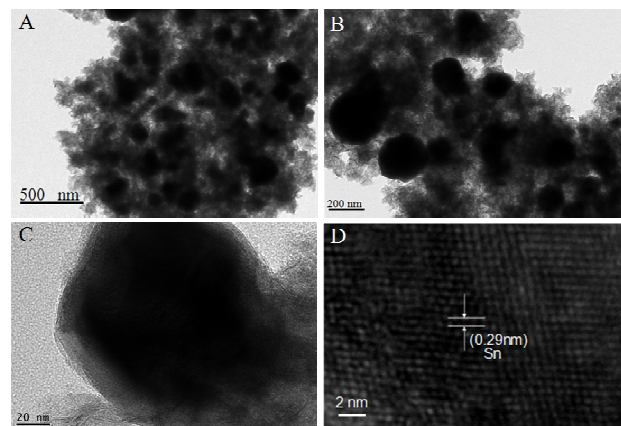
Fig. 8 TEM images of Sn/MoS_2/C composite

The cyclic voltammetry plot of the Sn/MoS_2/C composite is shown in Fig. 9 A, Which was collected at a slow scan rate of 0.1 mV s^{-1} in a potential window of 0.01 V-3.0 V vs Li^+/Li. In the first cathodic scan, the peaks located at 0.35V and 0.65V are referenced to the alloying process of lithium into tin forming Li_xSn, and the peak at the 0.8 V and could be assigned to the formation of a solid electrolyte interface (SEI) on the surface of Sn/MoS_2/C composite

and the cathodic peak at 1.65 V is attributed to the Li intercalation into the layered MoS_2.[20,28] A small broad peak at ~0.25 V is indicative of the reduction of Mo^{4+} to Mo metal, accompanied by the formation of Li_2S. Turning to the anodic process, a series of peaks between 0.4 V and 0.8 V are assigned to the de-alloying reactions of Li_xSn, and a dominant peak at around 2.35 V can be observed, which is ascribed to the oxidation of Li_2S to form S. It can be seen that the plot of the second and third scans are almost overlapped, indicating that good electrochemical reversibility of lithium storage in the $Sn/MoS_2/C$ composite starts from the second cycle.

To further demonstrate the electrochemical performance of the $Sn/MoS_2/C$ composite, Fig. 9 B exhibits cycle performance of $Sn/MoS_2/C$, MoS_2/C composite and Sn/C composite produced by hydrothermal method and annealed under 700 ^{o}C for 4h. As can be seen, the $Sn/MoS_2/C$ electrode shows superior cycling performance, delivering a high reversible capacity of 741.7 mAh g^{-1} after 150 cycles at a current density of 500 mA g^{-1}, which is about 89% of the reversible capacity in the third cycle. Moreover, their Coulombic efficiency is also very excellent, though the initial Coulombic efficiency only 50.1% which could be associated with the inevitable formation of SEI and decomposition of electrolyte.[17,21] However, which rapidly increases from 50.1% in the first cycle to 96.8% in the fourth cycles and remains above 98% during the subsequent cycles, indicating a facile insertion/extraction of lithium ions as well as efficient transport of electrons and ions in the $Sn/MoS_2/C$ composite. In contrast, a lower reversible capacity (~525 mAh g^{-1}) of the MoS_2/C composite is delivered at the end of 150 cycles under a current density of 500 mA g^{-1}. As for the Sn/C composite, it exhibits very fast capacity fading and have a very low reversible capacity of ~ 330 mAh g^{-1} after the 150th cycle. Therefore, the $Sn/MoS_2/C$ composite demonstrates remarkably higher reversible capacity and cycling stability, which is ascribed largely to the strong synergistic effect between the layer-structure MoS_2 nanosheets and the amorphous carbon coating layer. During the charge and discharge process, the MoS_2 nanosheets and carbon coating layer are very beneficial for the growth of a stable SEI film and thus can prevent the rupture of the SEI during cycling. In addition, the MoS_2 nanosheets with excellent mechanical flexibility, which can tightly anchor the Sn NPs and restrain the Sn NPs agglomeration to larger particles, which also can enhance the cycling stability. Moreover, the presence of sufficient void space between interconnected MoS_2 nanosheets not only allow fast lithium-ion diffusion but also effectively buffer the mechanical stress and volume change during the lithium intercalation/exfoliation.[37,38]

The rate performance of LIBs anode materials is highly crucial especially for high-power application in electric vehicles and hybrid electric vehicles.[1,2] Fig. 9 C. Compares to the rate capability of $Sn/MoS_2/C$ composite, MoS_2/C composite and Sn/C composite. During the first twenty cycles under current density at 100 mA g^{-1} and 200 mA g^{-1}, the capacity of $Sn/MoS_2/C$ composite kept decreasing from 1050 mAh g^{-1} to 895 mAh g^{-1}, and then became stable and delivered reversible capacities of 800 mAh g^{-1}, 732 mAh g^{-1} and 630 mAh g^{-1} at higher current density of 500 mA g^{-1}, 1 A g^{-1} and 2 A g^{-1}, respectively. When the current density was reduced to 100 mA g^{-1} again after cycling under high current densities, $Sn/MoS_2/C$ composite can still regain a reversible capacity near

1040 mAh g^{-1}, indicating that the $Sn/MoS_2/C$ composite remained very stable during the extended rate cycling process. However, for the MoS_2/C composite and Sn/C composite, the discharge capacity were 507 mAh g^{-1} and 247 mAh g^{-1} at the current density of 2 A g^{-1}, respectively. It is further proof that the $Sn/MoS_2/C$ composite exhibit improved rate capability and cyclic capacity retention.

However, In order to further confirming the superior performance of the $Sn/MoS_2/C$ composite, moreover, the long-term cycling stability at a high current density of 1 A g^{-1} of the $Sn/MoS_2/C$ electrode has also been explored, and the result is shown in Fig. 9 D. It is striking to note that the specific capacity can reach as high as 624.5 mAh g^{-1} at the current density of 1 A g^{-1} even after 500 cycles. The outstanding cycling stability and rate capability of the $Sn/MoS_2/C$ composite are achieved at high rate (1 A g^{-1}) are much larger than most of previously reported works on Sn nanostructures,[39,40] Sn/carbon[41-45] and Sn-graphene hybrids.[46,47]
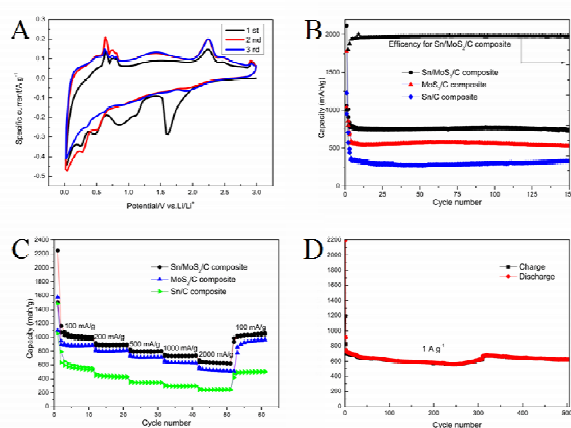
Fig. 9 (A) Cyclic voltammogram of the $Sn/MoS_2/C$ composite at a scan rate of 0.1 mV s^{-1}. (B) Cycling performance of the $Sn/MoS_2/C$ composite at a constant current density of 500 mA g^{-1}. (C) Rate-performance of the $Sn/MoS_2/C$ composite. (D) Cycling performance of the $Sn/MoS_2/C$ composite at a current density of 1 A g^{-1}.

The above results clearly confirm that our $Sn/MoS_2/C$ composite has superior cycle and rate performance, which can be ascribed to the following factors. First, the Sn NPs can offer a great deal of active sites for lithium ion storage and a short pathway for lithium ion transport, resulting in high reversible capacity and rate performance. Second, carbon coating layer and the MoS_2 nanosheets with excellent mechanical flexibility not only can prevent the Sn cores from directly contacting the electrolyte and alleviate the side reactions at the interface between Sn and electrolyte but also suppress the aggregation of Sn nanoparticles and accommodate the volume expansion, leading to structural and interface stabilization of Sn nanoparticles. Third, the ultra-thin MoS_2 nanosheets possess a high surface area for electrode/electrolyte interface and the diffusion length of electrons and ions can be effectively reduced,[47] and the MoS_2 nanosheets also can offer more defect sites, thus above can greatly enhance the capacity and rate performance. On the basis of the analyses presented above, it believe that the outstanding synergetic effect between the MoS_2 nanosheets and the Sn@C induces the superior lithium storage performance. However, to the best of our knowledge, the $Sn/MoS_2/C$ composite of electrochemical performance not best ever reported for a Sn-based lithium ion battery anode[20,49-54] because of the Sn nanparticles is too bigger in the

Sn/MoS$_2$/C composite, that can induced severe pulverization due to the dramatic volume change, that can lead to capacity loss.

Conclusions

In summary, novel Sn/MoS$_2$/C composite with Sn NPs encapsulated with layer-structure MoS$_2$ were successfully assembled through a facile hydrothermal and subsequent heat treat process. In this unique architecture, the carbon thin layer and the MoS$_2$ can accommodate the mechanical stress resulting from the serve volume change of Sn NPs during lithium ion insertion/extraction. As a result, long-term cyclic stability at high current density (a high capacity of 624.5 mAh g^{-1} is achieved at 1 A g^{-1} even after 500 cycles) and superior rate capability (1050 mAh g^{-1} at 100 mA g^{-1}, 895 mAh g^{-1} at 200 mA g^{-1}, 800 mAh g^{-1} at 500 mA g^{-1}, 732 mAh g^{-1} at 1 A g^{-1} and 630 mAh g^{-1} at 2 A g^{-1}) were achieved when Sn/MoS$_2$/C composite were used as an LIBs anode materials. All these observation demonstrates that the Sn/MoS$_2$/C composite can act as anode materials for high-performance lithium ion batteries.

Acknowledgements

Notes and references

1 L.Wang, X. M. He, J. J. Li, W. T. Sun, J. Gao, J. W. Guo and C. Y. Jiang, *Angew. Chem. Int. Ed.* , 2012, **51**, 9034-9037.

2 J. S. Zhu, D. L.Wang, L. B. Cao and T. F. Liu, *J. Mater. Chem. A*, 2014, **22**, 12918-12923.

3 H. Wu, N. Du, H. Zhang and D. R. Yang, *J. Mater. Chem. A*, 2014, **2**, 20510-20514.

5 T. Song, L. B. Hu and U. Paik, *J. Phys. Chem. Lett.* , 2014, **5**, 720-731.

6 X. K. Huang, S. Mao, J. B. Chang, J. W. Jiang and J. H. Chen, *Adv. mater.* , 2014, **26**, 4326-4332.

7 R. Z. Hu, W. Sun. Y. L.Chen, M. Q. Zeng and M. Zhu, *J. Mater. Chem. A* , 2014, **2**, 9118-9125.

8 Z. Q. Zhu, S. W.Wang, J. Du, Q. Jin, T. R.Zhang, F. Y. Cheng and J. Chen , *Nano. Lett.* , 2014, **14**, 153-157.

9 B. Liu, A. Abouimrane, Y. Ren, D. P. Wang, Z. Z. Fang and K. Amine, *Chem. Mater.* , 2012, **24**, 4653-4661.

10 S. H. Lee, J. H. Jung, Y. S. Lee, R. Mukherjee, N. Koratkar and K. Oh, *ACS Nano*, 2013, **7**, 4242-4251.

11 Y. Chen, B. H. Song, X. S. Tang, L. Lu and J. M. Xue, *J. Mater. Chem.* , 2012, **22**, 17656-17662.

12 J. Z. Chen, L. Yang, Z. X. Zhang, S. H. Fang and S. I. Hirano, *Chem. Commun.* , 2013, **49**, 2792-2794.

13 X. Y. Tao, R. Wu, Y. Xia, H. Huang, W. C. Chai, T. Feng, Y. P. Gan and W. K. Zhang, *ACS Appl . Mater. Interfaces*, 2014, **6**, 3696-3702.

14 H. S. Hou, X. N. Tang, M. Q. Guo,Y. Q. Shi, P, Dou and X. H. Xu, *Mater . Lett.* , 2014, **128**, 408-411.

15 L. M. Sun, X. H. Wang, R. A. Susantyoko and Q. Zhang, *Carbon*, 2015 **82**, 282-287.

16 X. Y. Zhou, Y. L. Zou and J.Yang, *J. Power sources*, 2014, **253**, 287-293

17 W. N. Ren, D. Z. Kong and C. W. Cheng, *ChemElectroChem*, 2014, **1**, 2064-2069.

18 Z. Tan, Z. H. Sun, H. H. Wang, Q. Guo and D. S. Su, *J. Mater. Chem. A*, 2013, **1**, 9462-9468.

19 Y. R. Zhong, M. Yang, X. L. Zhou, J. P. Wei and Z. Zhou, *Part. Part. Syst. Charact.* , 2015, **32**, 104-111.

20 J. Qin, C. N. He, N. Q. Zhao, Z. Y. Wang, C. S. Shi, E. Z. Liu and J. J. Li *ACS Nano*, 2014, **8**, 1728-1738.

21 D. N. Wang, X. F. Li, J. L. Yang, J. J. Wang, D. S. Deng, R.Y. Li and X. L. Sun, *Phy. Chem. Chem. Phy.* , 2013, **15**, 3535-3542.

22 C. D. Wang, Y. Li, Y. S. Chui, Q. H. Wu, X. F. Chen and W. J. Zhang, *Nanoscale,* 2013, **5**, 10599-10604.

23 J. S. Zhu, D. L. Wang, L. B. Cao and T. F. Liu, *J. Mater. Chem. A*, 2014, **2**, 12918-12923.

24 C. Wang, J. Ju, Y. Q. Yang, F. H. Liao, Z. J. Shi, F. Q. Huang and R. P. S. Han, *RSC. Adv.* , 2013, **3**, 21588-21595.

25 H. Hwang, H. Kim and J. Cho, *Nano Lett.* , 2011, **11**, 4826- 4830.

26 D. B. Kong, H. Y. He, Q. Song, B. Wang, W. Lv, Q. H. Yang and L. J. Zhi, *Energy Environ. Sci.* , 2014, **7**, 3320-3325.

27 Y. Chen, J. Lu, S. Wen, L. Lu and J. M. Xue, *J. Mater. Chem. A*, 2014, **2**, 17857-17866.

28 Y. Chen, B. H. Song, X. S. Tang, L. Lu and J. M. Xue, *small*, 2014, **10**, 1536-1543.

29 S. Han, Y. R. Zhao, Y. P. Tang, F. Z. Tan, Y. S. Huang, X. L. Feng and D. Q. Wu, *Carbon*, 2015, **81**, 203-209.

30 K. Chang, W. X. Chen, L. Ma, H. Li, F. H. Huang, Z. D. Xu and J. Y. Lee, *J. Mater. Chem. A*, 2011, **21**, 6251-6257.

31 L. Zhang and X. W. Lou, *Chem. Eur. J.* , 2014, **20**, 5219-5223.

32 K. Chang and W. X. Chen, *ACS Nano*, 2011, **5**, 4720-4728.

33 G. A. Elia, J. Wang, D. Bresser, J. Li, B, Scrosati, S. Passerini and J. Hassoun, *ACS Appl. Mater. Interfaces*, 2014, **6**, 12856-12961.

34 H. H. Zhao, H. Zeng, Y. Wu, S. G. Zhang, B. Li and Y. H. Huang, *J. Mater. Chem. A*, 2015, **3**, 10466-10470.

35 J. B. Ye, L. Ma, W. X. Chen, Y. J. Ma, F. H. Huang, C. Gao and J. Y. Lee, *J. Mater. Chem. A*, 2015, **3**, 6884－6893.

36 X. Y. Zheng, W. Lv, Y. Tao, J. J. Shao, D. W. Wang and Q. H. Yang, *Chem. Mater.* , 2014, **26**, 6896-6903.

37 B. J. Guo, K. Yu, H. Fu, Q. Q. Hua, R. J. Qi, H. L. Li, H. L. Song, S. Guo and Z. Q. Zhu, *J. Mater. Chem. A*, 2015, **3**, 6392-6401.

38 Y. Chen, J. Lu, S. Wen, L. Lu and J. M. Xue, *J. Mater. Chem. A*, 2014, **2**, 17857-17866.

39 A. Kohandehghan, K. Cui, M. Kupsta, E. Memarzadeh, P. Kalisvaart and D. Mitlin, *J. Mater. Chem. A*, 2014, **2**, 11261-11279.

40 H. Liu, R. Z. Hu, M. Q. Zeng, J. W. Liu and M. Zhu, *J. Mater. Chem.* , 2012, **22**, 8022-8028.

41 C. Y. Cui, X. G. Liu, N. D. Wu and Y. P. Sun, *Mater. Lett.* , 2015,**143**, 35-37.

42 Y. Q. Zhou, H. G. Wang, Y. Zeng, C. Li, Y. Shen, J. J. Chang and Q. Duan, *Mater. Lett.* , 2015, **155**, 18-22.

43 Y. G. Wang, B. Li, C. L. Zhang, H. Tao, S. F. Kang and X. Li, *J. power sources*, 2012, **219**, 89-83.

44 L. M. Sun, X. H. Wang, R. A. Susantyoko and Q. Zhang, *Carbon*, 2015, **82**, 282-287.

45 Z. X. Chen, Y. L. Cao, J. F. Qian, X. P. Ai and H. X. Yang, *J. Mater. Chem.* , 2010, **20**, 7266-7271.

46 Z. X. Chen, K. Xie and X. B. Hong, *Electrom. Acta*, 2014, **149**, 94-100.

47 F. Ye, B. T. Zhao, R. Ran and Z. P. Shao, *Chem. Eur. J.* , 2014, **20**, 4055-4063.

48 X. Y. Yu, H. Hu, Y. W. Wang, H. Y. Chen and X. W. Lou, *Angew. Chem. Int. Ed.* , 2015, **54**, 7395－7398.

49 J. Liu, Y. R. Wen, P. A. Van Aken, J. Maier and Y. Yu, *Nano. Lett*. , 2014, **14**, 6387-6392.

50 J. Liang, X. Y. Yu, H. Zhou, H. B. Wu, S. J. Ding and X. W. Lou, *Angew. Chem. Int. Ed.* , 2014, **53**, 12803－12807.

51 S. J. Ding, J. S. Chen and X. W. Lou, *Adv. Funct. Mater.* 2011, **21**, 4120-4125.